Proceedings of ASME Turbo Expo 2020
Turbomachinery Technical Conference and Exposition
GT2020
June 22-26, 2020, London, England

GT2020-15691

ATOMIZATION OF HIGH VISCOSITY LIQUIDS USING A TWO-FLUID COUNTERFLOW NOZZLE: EXPERIMENTS AND MODELING

Roshan Rangarajan[1], Hongyuan Zhang[1], Paul J Strykowski[1], Alison Hoxie[2]
Suo Yang[1], Vinod Srinivasan[1]

[1]University of Minnesota. Twin Cities
[2]University of Minnesota, Duluth

ABSTRACT

We study the enhanced atomization of viscous liquids by employing a novel two-fluid atomizer. The nozzle establishes a countercurrent flow configuration in which the gas and liquid are directed in opposite directions, establishing a two-phase mixing layer. Detailed measurements of droplet size distributions were carried out using laser shadowgraphy, along with high speed flow visualization. The measurements suggest that the liquid emerges as a spray with little further secondary atomization. The performance of this nozzle is compared to the 'flow-blurring' nozzle studied by other investigators for four test liquids of viscosity ranging from 1 to 133.5 mPa.s. The counterflow nozzle produces a spray whose characteristics are relatively insensitive to fluid viscosity over the range studied, for gas-liquid mass flow ratios between 0.25 and 1. To gain insight into the mixing process inside the nozzle, simulations are carried out using an Eulerian-Eulerian Volume of Fluid (VoF) approach for representative experimental conditions. The simulation reveals the detailed process of self-sustained flow oscillations and the physical mechanism that generate liquid filaments and final droplets.

Keywords: atomization, viscous liquids, spray, mixing layer

NOMENCLATURE

A	Spray surface area, eqn. (1)
d_{32}	Sauter mean diameter [m], eqn. (1)
d_0	Nozzle exit diameter [m]
d_1	Outer diameter of exit tube [m]
d_2	Inner diameter of outer tube of nozzle [m]
D	Exit diameter of flow-blurring nozzle [m]
g	Annular gap between liquid tube and housing [m]
H	Axia gap in flow-blurring nozzle [m]
L	Overlap length between liquid and exit tubes in counterflow nozzle [m]
$\dot{m}$	Mass flow rate [kg/s]
Oh	Ohnesorge number, eqn. (4)
$\dot{Q}$	Volumetric flow rate [m^3/s]
Re	Reynolds number, eqn (3)
V	Spray volume, eqn. (1)
We	Weber number, eqn. (2)
z	Axial distance from nozzle exit plane [m]

Greek Symbols

β	Air-liquid mass flow rate ratio, eqn.(6)
Δh	Enthalpy change, kJ/kg
μ	Liquid viscosity [mPa.s]
σ	Surface tension [N/m]
ρ	Fluid density [kg/m^3]

Subscripts

a	Air
l	Liquid

1. INTRODUCTION

Concerns over the impact of aviation transport on climate change have encouraged exploration of alternative renewable fuels which are not based on petroleum distillation. In particular, attention has focused on 'renewable diesel' which is the product of a variety of high-temperature, high pressure processes for transforming forest and agricultural residue into a hydrocarbon that is chemically similar to jet fuel. Jet fuel has been identified as a large and profitable market for the renewable biofuels industry [1]. Other non-traditional bioproducts, such as glycerol are also attractive in certain respects, namely their moderately high calorific value, and extremely low cost. While several issues remain to be solved before adoption of bio-oils for jet engine combustion is possible, such as low heating value and moderate oxygen content, the major challenge derives from their high viscosity (>25 cP), which results in poor atomization characteristics compared to jet fuel (~ 3 cP) or bio-diesel (6 cP) [2]–[4].A reduction in droplet size enables higher volumetric heat release rates and lower concentrations of pollutants in exhaust [4]. Currently, very little is understood about the atomization process of high viscosity fluids, and a few studies with conventional pressure-swirl and air-assist atomizer nozzle designs have concluded that these designs are unsuitable for high viscosity fluids [5]–[7]. Primary atomization in viscous fuels has been observed to produce fluid ligaments that are longer and persistent in the downstream direction, leading to poor secondary atomization into droplets [6].

This study investigates the spray produced by a novel high-efficiency atomizer. We characterize the droplet distribution in terms of the Sauter Mean Diameter (d_{32}), a derived parameter which represents the ratio of the total volume of the spray to its total surface area,

$$d_{32} = \frac{\sum n_i d_i^3}{\sum n_i d_i^2} = \frac{6V}{A} \tag{1}$$

where V and A are the volume and surface area of the spray respectively. Liquid properties that govern the atomization process are represented through two quantities that describe the interplay of inertia viscosity and surface tension: the Weber and Reynolds numbers:

$$We = \frac{\rho U^2 d}{\sigma} \tag{2}$$

$$Re = \frac{\rho U d}{\mu_l} \tag{3}$$

Alternatively, one can use the two quantities above along with the Ohnesorge number, which is independent of dynamical quantities:

$$Oh = \frac{\mu}{\sqrt{\rho_l \sigma d}} \tag{4}$$

where σ is the surface tension, μ is the liquid dynamic viscosity and d is a relevant length scale, usually the nozzle exit diameter.

The process of jet breakup and spray formation has been exhaustively covered in several reviews [8][9]; it is generally understood that in order to break up a liquid jet emerging from a nozzle, high rates of external mean shear are required to overcome surface tension. A typical gasoline-based fuel in a swirl atomizer emerges in the form of a thin conical sheet that develops instabilities with wavelengths of the order of the shear layer thickness in the external flow [10]. The resulting fluid ligaments then break up further through a Rayleigh-Taylor instability [11] into droplets. These droplets are further deformed under the influence of shear and droplet-droplet collisions, and undergo fragmentation and secondary atomization [12]. The instability mechanisms mentioned above are suppressed as the liquid viscosity increases, since high viscosity transmits surface shear into the interior of the fluid and resists liquid breakup.

Internal mixing nozzles employ a different strategy, namely, creation of a two-phase mixture in a chamber at moderate pressures. The two-phase flow undergoes strong acceleration near the nozzle exit, causing rapid bubble expansion and fragmentation of liquid ligaments in the near-field of the nozzle exit. Effervescent atomization [13], [14] is a process in which bubbles are introduced into the liquid upstream of the nozzle exit, and has been extensively documented. When an annular flow is established in the nozzle exit, atomization is highly efficient, producing small droplets from viscous liquids. However, performance is known to sharply deteriorate when the flow regime changes, reducing operational flexibility. The 'flow-blurring' nozzle introduced by Ganan-Calvo [15], and systematically studied by Agrawal and co-workers [16][17] is a design that combines the advantages of both internal and external mixing nozzles through the bifurcation of atomizing air both within and outside of the exit region of the nozzle. This process creates intense shear layers between the liquid and gas in the fuel supply tube, producing a 2-phase flow exiting the nozzle orifice. Gañan-Calvo showed this atomization technique has a smaller delivery penalty over other pneumatic atomization techniques. Crucially, the flow-blurring phenomenon has been found to occur for a very specific condition, H/D < 0.25 where H and D are the nozzle-plate spacing and orifice diameter. A range of correlations for the performance of effervescent atomizers can be found in surveys by Konstantinov [14] and it can be seen that exponents for the scaling of d_{32} with parameters such as gas density, liquid viscosity, and air-liquid mass flow ratio can vary significantly. It is important to note that this empiricism is the result of the complex dynamics of two-phase mixing in internal mixing nozzles. This makes them less amenable to modeling approaches that are well-established for co-flowing streams found in air-assist nozzles.

In this work, we rely on insights from linear stability theory to establish a flow configuration that relies on turbulent stresses, as opposed to mean shear, to overcome viscous stresses at the fluid/gas interface and promote atomization. The performance of the counterflow nozzle studied here has been documented elsewhere [18], [19] for water as a working fluid. Here we focus on the effects of fluid viscosity. Countercurrent shear layers are known to display 'global modes' characterized by a sharp onset of self-sustained oscillations and a loss of similarity in shear layer profile development, once the velocity ratio between the two counterflowing streams is increased beyond a critical value [20], [21]. Other globally unstable systems that display such behavior include bluff-body wakes

[22], variable density [23][24] and variable viscosity flows [25]. Strong connections have been shown between the steep onset of experimentally observed global modes with change in a control parameter (typically a velocity or density ratio) and the absolute/convective nature of local velocity profiles in the flow [26]–[28]. In particular, the breakdown of a laminar counterflowing mixing layer and the emergence of high levels of turbulent stress for supercritical velocity ratios is known to be independent of the fluid viscosity, and has been exploited to dramatically increase heat release rates in combustion of prevaporized jet fuel[29]. We anticipate that this weak dependence on viscosity, which has been documented for single-phase mixing layers, will be somewhat mediated by the effects of surface tension in a two-phase mixing layer. There has been some work documenting the onset of absolute instability in co-flowing two-phase mixing layers [30], [31]; the countercurrent mixing layer has not received much attention.

Figure 1(a) shows a sketch of the near-tip geometry of the 'counterflow' (CF) nozzle recently developed at the University of Minnesota [30]. The spray exits to the ambient through a hypodermic needle of inner diameter d_0 and outer diameter d_1. The liquid supply line of inner diameter d_2 partially overlaps with the needle in the axial direction by a distance L (L is negative for an axial clearance). Air flows through the annular space formed between the liquid supply tube and an outer housing. The axial overlap of length L and annular gap g= (d_2-d_1)/2 between the needle and the liquid supply line causes the air flow to reverse its direction and also controls the velocity magnitude.

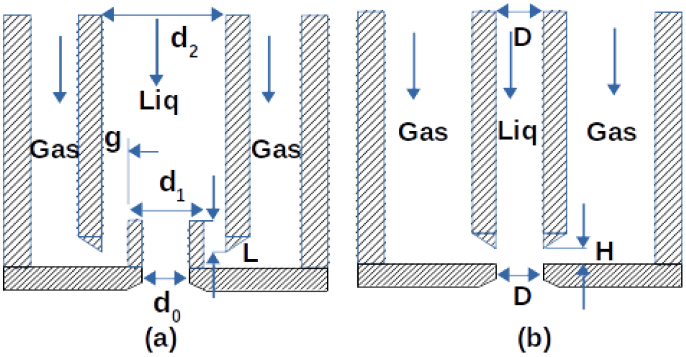

Figure 1. Sketches of the nozzle geometries studied: (a) counterflow (CF) and (b) flow-blurring (FB) nozzle.

The overlap region is long enough that the reversed air stream travels upstream for several hydraulic diameters before encountering the liquid stream, potentially establishing a smooth velocity profile. Above the needle, the strong countercurrent shear established at the interface promotes mixing, and the liquid is forced out of the nozzle tip as a spray. The dimensions of the CF nozzle studied were d_0=1.56 mm, d_1=2.08 mm, d_2= 2.51 mm and L = 1 mm. For comparison, the performance of a flow-blurring (FB) nozzle with the same exit diameter of D=1.56 mm was also documented. The flow-blurring nozzle shown in fig. 1(b) had an axial gap-to-diameter ratio of H/D=0.2, ensuring that it was operating in the flow-blurring regime.

A preliminary analysis of the flow, described in detail elsewhere [32] assumes that the air stream bubbles into the mixing chamber with sufficient momentum as to render the flow globally unstable. The bubble diameters are assumed to be of the order of the annular gap 'g' given by

$$g = (d_2 - d_1)/2 \quad (5)$$

Knowledge of the air mass flow rate enables calculation of the generation rate of air bubbles, which are assumed to be linked to the number of fluid ligaments in the interstitial spaces between bubbles. Knowing the liquid mass flow rate, and further assuming that these ligaments, when exiting the nozzle, retain the same length scale, a 'mean' droplet diameter d_m is derived in ref. [32] as:

$$\frac{d_m}{g} = c\left(\frac{\rho_a}{\rho_l}\right)^{1/3}\beta^{-1/3} \quad (6)$$

where the subscripts a and l represent atomizing air and liquid respectively, and β is the air-liquid mass flow ratio:

$$\beta = \frac{\dot{m}_a}{\dot{m}_l} = \frac{\rho_a \dot{Q}_a}{\rho_l \dot{Q}_l} \quad (7)$$

which is calculated by measuring the input mass flow rates. In ref. [32], data were taken using multiple gases (helium, argon, air) in order to isolate the effects of gas density from the pressure-influenced effects of gas inertia, and equation (5) was observed to be an accurate fit. The prefactor c in equation (3) is a constant of order unity, and is assumed to embody the effects of liquid properties, through the Ohnesorge number Oh, and nozzle geometry.

2. MATERIALS AND METHODS

The approach followed in this study was to perform laser shadowgraphic measurements to obtain detailed droplet statistics downstream of the nozzle exit for a range of fluid viscosities from 1 cP to 133.5 cP. The fluids used, along with relevant physical properties, are listed in table 1. Liquid density and viscosity were measured in the Polymer Characterization Laboratory, at the University of Minnesota, while surface tension data were taken from the literature [33][34]. High speed flow visualization was conducted to check for any sustained frequencies in the spray, which can be correlated with computational simulations of the internal dynamics of the nozzle.

Liquid	Density (kg/m^3)	Viscosity (mPa.s)	Surface Tension (mN/m)	Oh
Water	998	0.9	72	0.0027
Propylene glycol (PG)	1042	49.3	36	0.23
Glycerol/water (85%-15% v/v)	1229	133.5	66	0.45

Table 1. Properties of fluids used in the experiment.

2.1 Experimental Method

The experimental setup is shown schematically in figure 2. A gear pump is used to deliver a known liquid flow rate into the nozzle. The air flow is delivered from the building

supply through a pressure regulator and valve, and the flow rate is measured using a mass flow meter (Omega). Air supply pressures of up to 7 bar and flow rates of up to 80 g/s can be attained. The beam from a pulsed Nd:YaG laser (Beamtech Vlite 200, 532 nm, 200 mJ/pulse, pulse-width ~ 6 ns) operating at 15 Hz is expanded using optics and further diffused by a plastic sheet which serves as a backlight against which droplets are illuminated. Images of size 24 megapixels are acquired using a Canon EOS 77D camera coupled to a K2 Distamax long working-distance microscope with a CF4 objective lens. This produces an image with a magnification of 0.55 microns/pixel, and a field of view of approximately 3.3 x 2.2 mm. Image processing is performed using the software ImageJ. The majority of droplets were sufficiently small that depth-of-field corrections were not considered necessary. Droplet statistics were extracted by ensemble averaging over 1000 images, which typically yielded in excess of 20,000 droplets in all cases considered. Droplets below a diameter of 3.5 μm (7 px by 7 px) were ignored when calculating statistics. For this data reduction procedure, the calculated droplet diameter changed by less than 1 μm when half the images were considered, and this value is taken as a measure of uncertainty. Flow visualization was conducted using a Photron Mini AX200 high speed camera operating at 3000 frames/second.

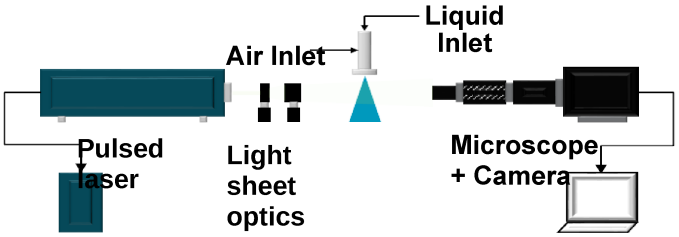

Figure 2. Sketch of experimental setup

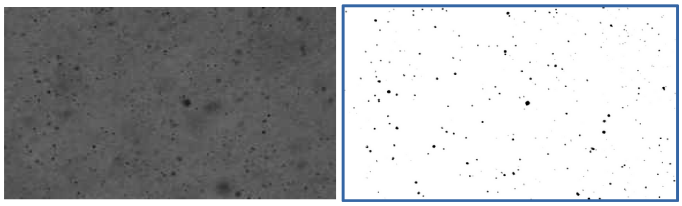

Figure 3. (a) Raw image acquired at β=0.5, z/d_0= 30 for water, and (b) corresponding processed image.

Figure 3 shows a representative image taken at an axial location 30 diameters downstream (z/d_0=30) of the exit plane, along with its processed counterpart for water at β =0.5. Droplets are identified by applying a threshold to the image grayscale value at each pixel, marking bright areas as the background and dark areas as droplets. The variation in illumination across multiple images is eliminated by normalizing the brightest and darkest portions of the image to have the same bit value, so that the process of identifying droplets is not sensitive to the value of threshold used. While shadowgraphic droplet sizing can introduce error due to droplets being out of focus, and, depending on optics, finite thickness of the depth-of-field, these errors are small when the droplet sizes are small [35], [36]. No attempt is made, therefore, to correct the drop diameter values obtained in the current study.

For a fixed liquid volume flow of 60 ml/min, the air flow rate was adjusted to produce the desired value of β, gas-liquid mass ratio ranging from 0.25 to 1. All other dynamic quantities, such the liquid and air pressures get determined by the mixing process in the nozzle chamber. All pressures were measured at the inlet to the nozzle assembly.

2.2 Numerical Method

In this study, the two-dimensional (2D) simulations are conducted by the "compressibleMultiphaseInterFoam" solver in the OpenFOAM-6 toolbox **[37]**. This solver is based on Eulerian-Eulerian volume of fluid (VOF) framework. Both gas and liquid are considered as compressible fluids, and surface tension is taken into account. Bounded Euler implicit scheme is used for time integration. Gaussian integration based on linear interpolation is used for finite volume discretization of spatial gradient terms and divergence terms, and Van Leer limiter is used to remove the spurious numerical oscillations near the interfaces from the divergence terms (i.e., nonlinear convection terms).

The grid of the simulation is shown in figure . The grid is clustering towards the wall and shear layers. At the outlet, the horizontal grid resolution is approximately 51.6 μm. At the air inlet, the horizontal grid resolution is approximately 21.59 μm. At the wall, the horizontal grid resolution is approximately 26.6 μm. The vertical grid resolution is approximately 100 μm. No sub-grid (SGS) model is used in this study.

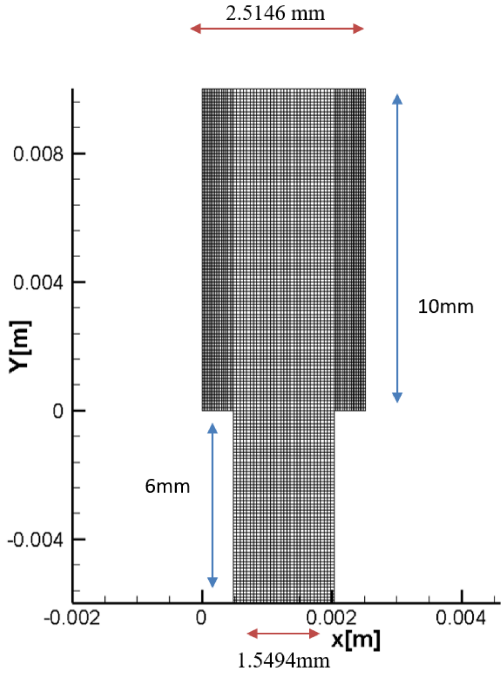

Figure 4. Grid used for simulations.

The liquid inlet velocity is fixed as 0.2 m/s, and the air inlet velocity is calculated accordingly based on the β (air-to-

liquid mass flow rate ratio). No-slip boundary condition is applied at the wall. Zero normal velocity gradient is applied as the outlet boundary condition. Pressure is calculated as perfect gas in the gas phase and as perfect fluid in the liquid phase. Temperature is fixed as 300 K without solving the energy equation to make the numerical solver more stable and robust. The simulation is initialized with pure liquid at 1 atm in the whole domain.

3. RESULTS AND DISCUSSION

3.1 High Speed Flow Visualization

Figure 5 shows a snapshot of the flow emerging from the nozzle. Droplets appear to emerge directly from inside the nozzle. Within a downstream distance of two diameters, there are no large ligaments visible, though some large drops break off and continue to fission downstream. The major difference seems to be that this behavior is not sensitive to operating conditions, i.e. there is no upper bound on the value of gas-liquid ratios that can be reached for which this behavior is observed.

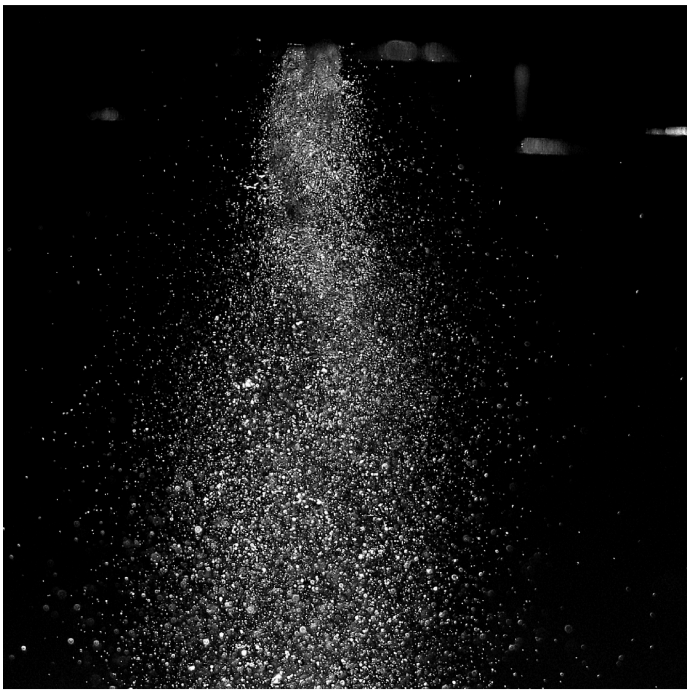

Figure 5. High-speed visualization of the spray exiting the counterflow nozzle as a collection of drops for a water flow rate of 60 ml/min, β=0.25.

Figure 6 shows the corresponding image for the FB nozzle operating at the same conditions. In this case, the spray seems sparser due to the presence of larger droplets. A crown of liquid near the exit orifice is visible, out of which droplets break off. This is qualitatively similar to effervescent atomization.

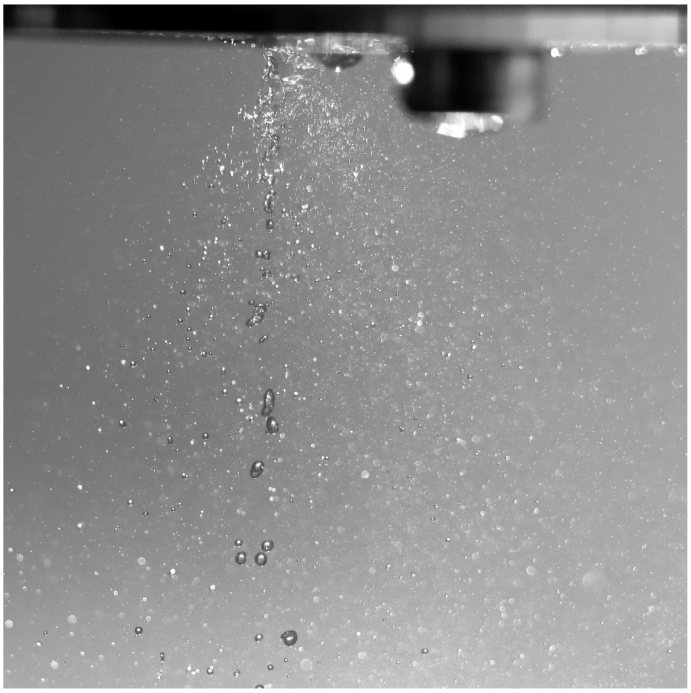

Figure 6. High-speed visualization of the spray exiting the flow-blurring nozzle for a water flow rate of 60 ml/ min, β=0.25.

3.2 Droplet Measurements

Figure 7 shows the histogram of the droplet diameter distribution, as well as the histogram of the volume distribution. The number distribution peaks sharply at diameters less than 10 μm; the number-weighted volume distribution has a maximum around 16 μm. The cumulative volume fraction of the droplet distribution for water at β=0.5 (fig. 8) indicates that 50% of the spray volume is contained in droplets that are smaller than 36 μm, while 90% of the volume is under 74 μm.

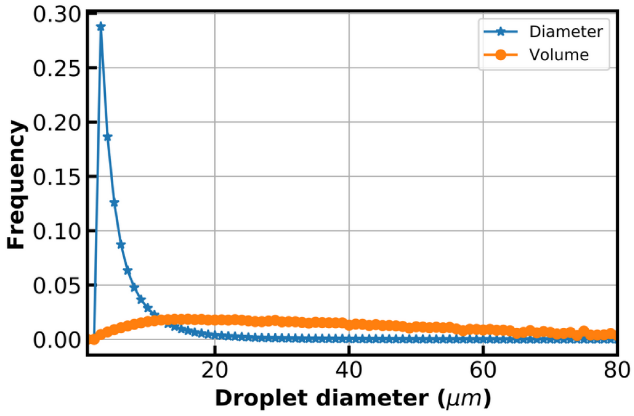

Figure 7. Histograms of droplet diameter and volume distribution in a water spray at z/d_0=30 for the CF nozzle, β=0.5

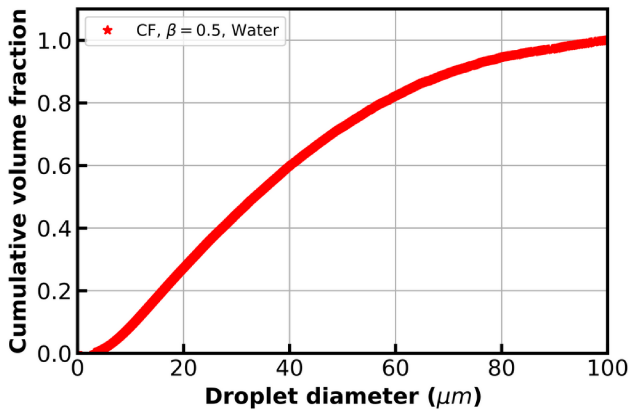

Figure 8. Cumulative volume fraction for a water spray at z/d_0=30 for the CF nozzle, β=0.5

Figure 9 shows the values of d_{32} as a function of the mass flow ratio and atomized liquid for the two nozzle geometries. Several observations may be made about the behavior of the droplet diameters produced. First, over the range of β studied, the values of d_{32} produced by the CF nozzle are not a strong function of the liquid properties. The increase in d_{32} due to an increase in viscosity of two orders of magnitude is no more than 20 % at the lowest β studied. By contrast, the mean diameters produced by the FB nozzle for low values of β are quite sensitive to liquid properties, increasing five-fold as the value of β is reduced from 1 to 0.25. Data were not acquired using the FB nozzle for the highest viscosity liquid.

The insensitivity of the spray produced by the CF nozzle to liquid viscosity is consistent with the role of turbulent stresses in promoting mixing inside the chamber, resulting in a bubbly flow exiting the chamber. Presumably, there is an upper limit to the insensitivity; one that is not explored in this study. Interestingly, the difference in performance between the two nozzles significantly decreases as the β increases. It is possible that as β increases, a greater portion of the air flow supplied to the FB nozzle is diverted upstream into the liquid tube, resulting in an effect similar to that of the CF nozzle, albeit in an uncontrolled manner. The data suggest that at large values of β, both nozzles asymptote to the same value of d_{32}.

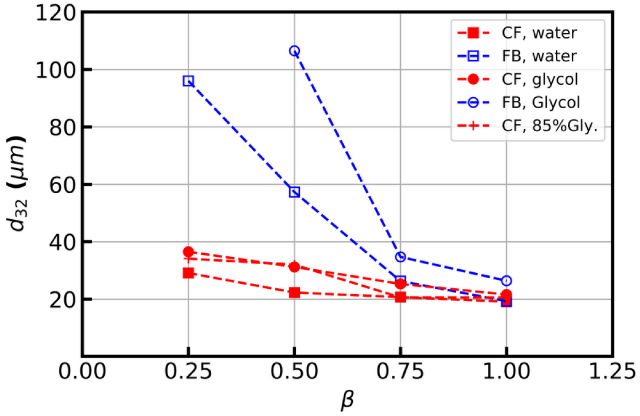

Figure 9. Dependence of Sauter mean diameter on fluid viscosity and mass flow ratio for the two nozzles considered.

We examine the scaling of d_{32} with β in greater detail in fig. 10. Power law fits of d32 with respect to β yield exponents of -0.30, -0.37 and -0.43 for water, glycol and the 85% glycerol solution respectively. Noting the proximity of these values to -1/3, we fit the data to power laws with an exponent of -1/3. Best fits to -1/3 power laws for the three liquids after accounting for density ratio effects given by eqn (1) yields pre-factor values of 0.77, 1.0 and 0.99 respectively, which are plotted in fig. 9. The data are consistent with the scaling proposed in eqn (1), suggesting the plausibility of the assumptions of the model, such as incompressible mixing at constant pressure, and formation of interstitial liquid ligaments between bubbles.

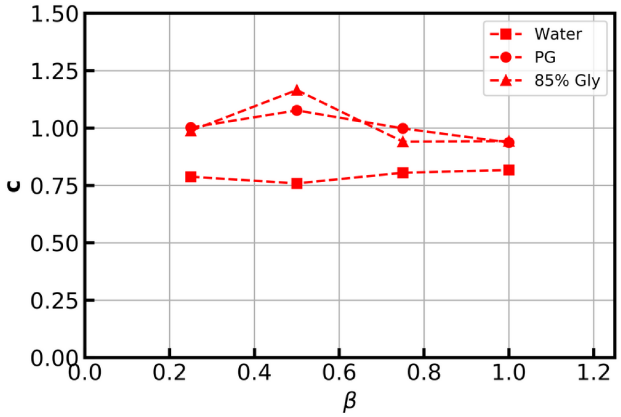

Figure 10. The constant prefactor from eqn (1), evaluated for all three liquids.

Given that the liquid flow rates and geometry are fixed, the variation of the pre-factor reflects the combined effects of surface tension and viscosity. However, noting from table 1 that surface tension variation is not large and therefore the Ohnesorge number may not be appropriate control parameter, we choose to work with a parameter that solely reflects the liquid viscosity, namely the liquid Reynolds number based on d_0 as the length scale and the liquid velocity. The liquid velocity used in the Reynolds number calculation is based on the assumption of flow through a cylindrical area of diameter d_2, with known density and flow rate Fitting a power law to the constants shown in fig, 10 yields an overall correlation (fig. 11) that clearly shows the weak dependence of the mean droplet diameter on the viscosity:

$$\frac{d_{32}}{g} = 1.10 Re_l^{-0.048} \left(\frac{\rho_a}{\rho_l}\right)^{1/3} \beta^{-1/3} \qquad (8)$$

Figure 11 plots all values of d_{32} obtained in this study using the CF nozzle against the observed functional quantity derived from the individual scaling laws. Work currently underway investigates the extension of this scaling to liquids with higher viscosities and other values of surface tension.

Finally, we address the question of the pressure drop penalty associated with injecting the atomizing air into the liquid stream. Internal mixing nozzles have a higher pressure drop in

the air stream due to the coupling between liquid and air pressures in the mixing chamber, unlike an external mixing chamber in which the fluids mix at ambient pressure. Figure 12 plots the air pressure drop against the air flow rate, for various liquid flow rates. At the highest water flow rates of 70 ml/min and β=1.2 (air flow rate of 1.4 g/s), an inlet pressure of 5 bar is required. However, given that efficient atomization occurs at lower air flow rates, and droplet sizes are ~ 30 μm even for β=0.5, a more representative value for the pressure drop for a liquid flow rate of 60 ml/min and β=0.5 (0.5 g/s) is substantially smaller at about 1 bar. While these values will change as a result of increased mass flow rates in real applications, we also anticipate that the dimensions can be changed accordingly to reduce pressure drop. It is notable that the pressure drop is also a very weak function of viscosity, attesting to the minimal influence of mean viscous stresses on the atomization process.

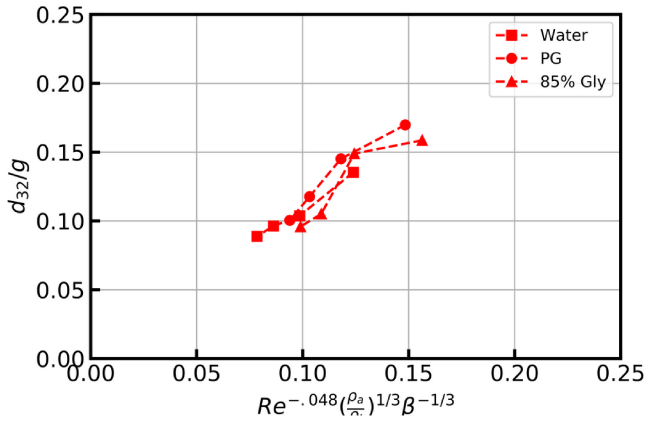

Figure 11. Scaling correlation that includes effects of liquid viscosity and bubble packing inside nozzle chamber.

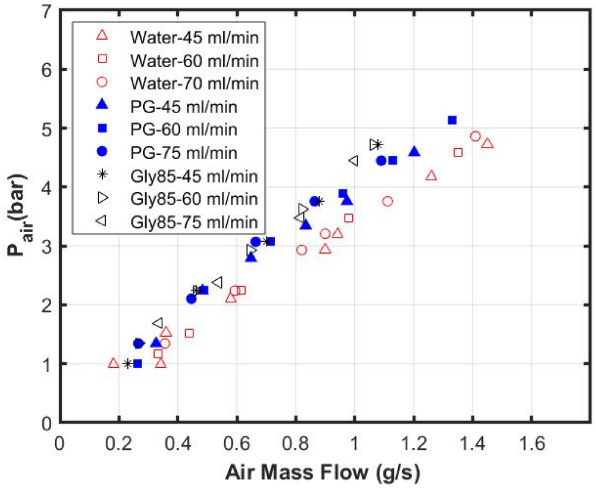

Figure 12. Inlet pressure (bar) of air stream through the counterflow nozzle as a function of air mass flow rate (g/s) for multiple liquids and flow rates.

In figure 13 we examine the efficiency of atomization, given by the expression

$$\eta = \frac{\sigma \dot{A}}{\dot{m}_l \Delta h_l + \dot{m}_a \Delta h_a} \sim \left(\frac{6\sigma}{\beta \Delta p_a d_{32}}\right)\frac{\rho_a}{\rho_l} \tag{9}$$

where the numerator refers to the rate of generation of liquid surface area, and the denominator is the work input. Using the definition of d_{32} from eqn (1) on a time rate basis, and neglecting the liquid pumping work, one obtains the second part of equation (9). The actual values of this quantity are less than 1%, with values of about about 0.2% for water, and decreasing further as viscosity is increased. For a fixed viscosity and given droplet diameter, the CF nozzle has a higher efficiency than the FB nozzle, within the range of values considered.

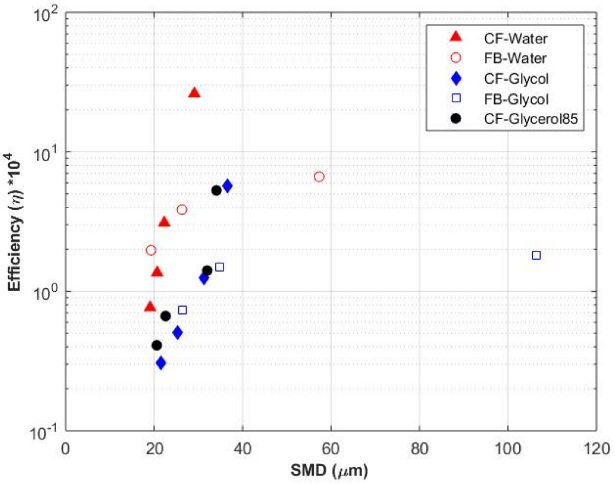

Figure 13. Surface area generation efficiency characteristics of the two nozzles for the test liquids considered.

3.2 Computational Results

Computations were performed in order to provide additional insight into the likely mechanisms governing the observed spray behavior. Direct validation of the experimental results such as spray characteristics are not possible due to the lack of detailed, spatially resolved measurements of quantities at the nozzle exit. Therefore, we restrict ourselves to simulating the internal dynamics of the nozzle in order to provide mechanistic understanding rather than attempting to match spray integral quantities.

Effect of β

To test the effect of β, four β values (0.25, 0.5, 0.75, 1.0) are simulated at the same viscosity of 1 cP. For each case, a periodic stable-unstable atomization process is observed. As an example, fig. 14 shows the periodic atomization process at β=0.5. At stable moment, liquid stream is located near the center of the outlet tube. Due to the high velocity difference between liquid and air, the stream gradually becomes unstable due to the Kelvin–Helmholtz instability. The unstable liquid stream begins to undergo an asymmetric flapping instability

that is typically observed in planar shear layers, impinges on the wall, resulting in breakdown of the stream and enhanced atomization. After sufficient oscillation, collision, and fragmentation, the original liquid stream is completely atomized, and a new stable stream grows up from the top to enter the next period.

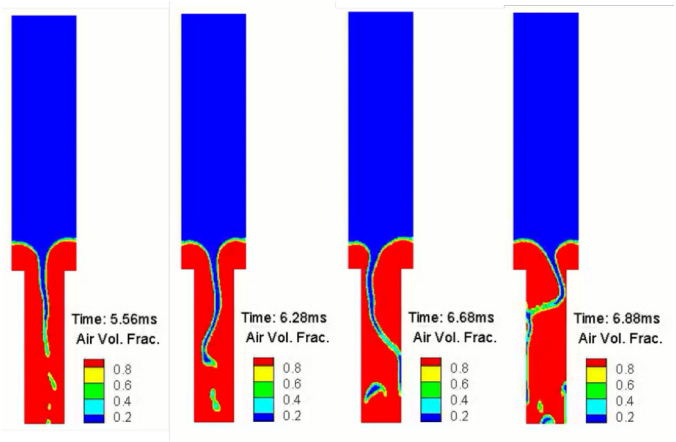

Figure 14. Snapshots of air volume fraction for the periodic atomization process at β=0.5 and viscosity of 1 mPas.

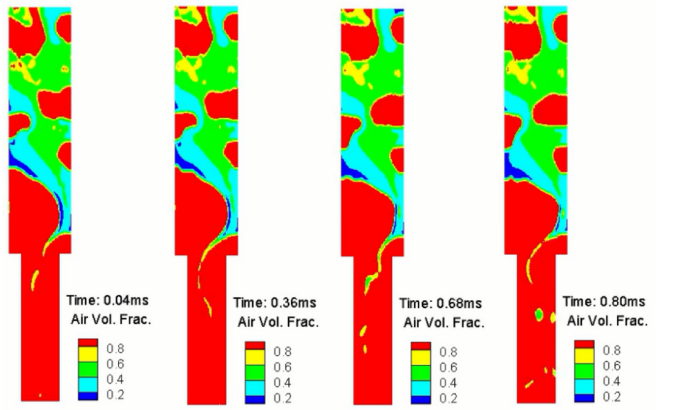

Figure 15. Snapshots of air volume fraction for the periodic atomization process at β=1.0 and viscosity of 1 cP.

The major effect of β on the atomization process is the frequency of the aforementioned periodic process. The frequencies are 292 Hz, 315 Hz, 985 Hz, and 1750 Hz for β of 0.25, 0.5, 0.75, and 1.0, respectively. Therefore, the frequency is increasing with β almost exponentially, which significantly enhances the atomization.

For β up to 0.75, the atomization is purely due to the Kelvin–Helmholtz instability, and air bubbles are not observed in the simulation results. In contrast, as shown in fig. 15, when β is further increased to 1.0, big bubbles start to show up in the upstream mixing region due to the high inertia of the air jet. There are some regions with air volume fraction between 0 and 1, indicating a large number of bubbles below the grid resolution. Nevertheless, all these bubbles later merge with the primary air streams and are not preserved in the flow through the exit tube, and therefore do not help the atomization process. The atomization process remains controlled by the Kelvin–Helmholtz instability.

Effect of viscosity

To test the effect of viscosity, three viscosity values (1 cP, 20 cP, 40 cP) are simulated at the same β of 0.5 and shown in figure 16. Similar to previous cases, a periodic stable-unstable atomization process is observed for each value of viscosity. No apparent morphological differences can be observed between different viscosities. The atomization frequencies are 315 Hz, 318 Hz, and 283 Hz for 1 cP, 20 cP, and 40 cP, respectively. So very high viscosity can reduce the frequency and weaken the atomization. In other words, the liquid stream is unlikely to undergo fragmentation if the viscosity is high. But the relationship between frequency and viscosity is not monotonic as 20 cP actually has higher frequency than 1 cP. Overall, the effect of viscosity on the atomization frequency is weak.

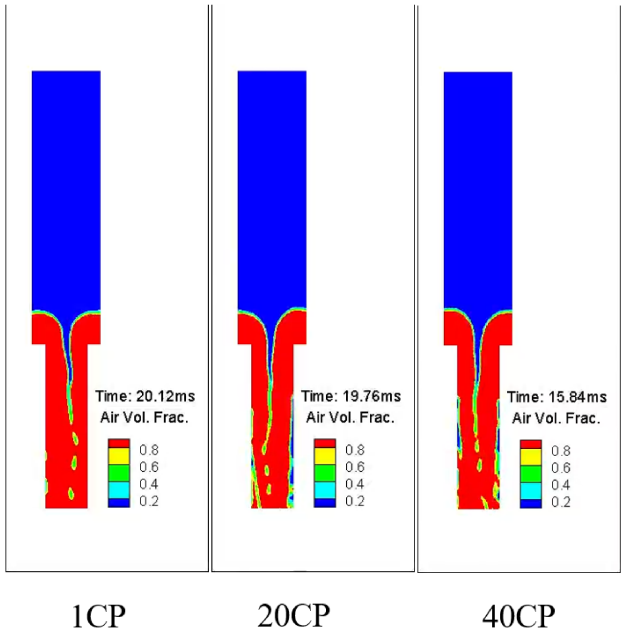

Figure 16. Snapshots of air volume fraction to compare the effect of viscosity at β=0.5.

Simulations for test liquids

To compare the result of three different kinds of liquid, water, glycol and 85% glycerol, three simulations are conducted at the same β of 0.8 and is shown in fig 17. Similar to the results at β = 0.75, the atomization is purely due to the Kelvin–Helmholtz instability, and air bubbles are not observed in the simulation results. Comparing β of 0.75, three results, with larger β, have larger regions filled with air at the air inlet. Although the three test liquids have different viscosity and density, they show no apparent morphological difference in the results. The atomization frequencies are 1228 Hz, 1260 Hz, and 1036 Hz for water, glycol, and 85% glycerol. The frequencies agree with the previous results. All three frequencies are between the result of β =0.75 and β =1.0, which shows the

dominant effect of β. Despite the significant difference in viscosities of the three liquids, water and glycol have similar atomization frequencies, while 85% glycerol displays a lower frequency. We suspect that the difference is mainly due to the higher density of 85% glycerol compared to the density of water and glycol. Overall, the atomization process is dominated by β, and liquid properties have a relatively weak influence on the atomization.

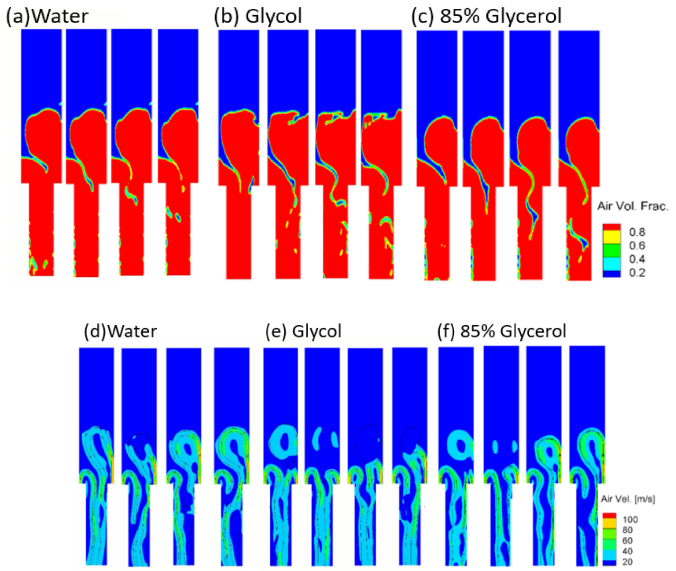

Figure 17. Snapshots of distribution of (a-c) air volume fraction and (d-f) velocity for the three test liquids at β=0.8 for a volume flow rate of 60 ml/min.

4. CONCLUSION

The major findings from this study are:

1. The counterflow nozzle generates a spray with Sauter mean diameters that are very weakly sensitive to changes of viscosity over two orders of magnitude. This is consistent with the hypothesis that counterflowing velocity and density profiles establish a flow with high levels of turbulent stresses.
2. The mixing process appears essentially incompressible, with a scaling that depends primarily on the volumetric flow rates of atomizing air.
3. High-fidelity simulations suggest that the primary mechanism responsible for spray formation is a Kelvin-Helmoltz-type instability of the liquid jet inside the nozzle, rendering it insensitive to liquid viscosity.

5. REFERENCES

[1] W. C. Wang and L. Tao, “Bio-jet fuel conversion technologies,” *Renew. Sustain. Energy Rev.*, vol. 53, pp. 801–822, Jan. 2016.

[2] K. Sipilä, E. Kuoppala, L. Fagernäs, and A. Oasmaa, “Characterization of biomass-based flash pyrolysis oils,” *Biomass and Bioenergy*, vol. 14, no. 2, pp. 103–113, 1998.

[3] M. W. Nolte and M. W. Liberatore, “Viscosity of biomass pyrolysis oils from various feedstocks,” *Energy and Fuels*, vol. 24, no. 12, pp. 6601–6608, 2010.

[4] A. H. Lefebvre and D. R. Ballal, *Gas Turbine Combustion, Alternative Fuels and Emissions*, 3rd ed. CRC Press, 2010.

[5] A. Pozarlik, A. Bijl, N. Alst, R. Pander, and E. Bramer, “Combustion of pyrolysis oil blends with diesel fuel in a micro gas turbine,” in *24th European Biomass Conference and Exhibition, 6-9 June 2016, Amsterdam, The Netherlands*, 2016.

[6] J. L. H. P. Sallevelt, A. K. Pozarlik, and G. Brem, “Characterization of viscous biofuel sprays using digital imaging in the near field region,” *Appl. Energy*, vol. 147, pp. 161–175, 2015.

[7] J. Gudde, “The impact of spray quality on pyrolysis oil combustion in gas turbines,” *Univ. Twente*, 2013.

[8] S. P. Lin and R. D. Reitz, “Drop and spray formation from a liquid jet,” *annu. Rev. Fluid Mech.*, vol. 30, no. 1, pp. 85–105, 1998.

[9] J. C. Lasheras and E. J. Hopfinger, “Liquid Jet Instability and Atomization in a Coaxial Gas Stream,” vol. 32, pp. 275–308, 2000.

[10] A. Lozano and F. Barreras, “Longitudinal instabilities in an air-blasted liquid sheet,” *J. Fluid Mech.*, vol. 437, pp. 143–173, 2001.

[11] D. D. Joseph, J. Belanger, and G. Beavers, “Breakup of a liquid drop suddenly exposed to a high speed airstream,” *Int. J. Multiph. Flow*, vol. 25, pp. 1263–1303, 1999.

[12] D. R. Guildenbecher, C. López-Rivera, and P. E. Sojka, “Secondary atomization,” *Exp. Fluids*, vol. 46, no. 3, pp. 371–402, 2009.

[13] S. D. Sovani, P. E. Sojka, and A. H. Lefebvre, “Effervescent atomization,” *Prog. Energy Combust. Sci.*, vol. 27, no. 4, pp. 483–521, 2001.

[14] D. Konstantinov, R. Marsh, P. Bowen, and A. Crayford, “Effervescent atomization for industrial energy - Technology review,” *At. Sprays*, vol. 20, no. 6, pp. 525–552, 2010.

[15] A. M. Gañán-Calvo, “Enhanced liquid atomization: From flow-focusing to flow-blurring,” *Appl. Phys. Lett.*, vol. 86, no. 21, pp. 1–3, 2005.

[16] B. M. Simmons and A. K. Agrawal, “Spray Characteristics of a Flow-Blurring Atomizer,” *At. Sprays*, vol. 20, no. 9, pp. 821–835, 2010.

[17] B. M. Simmons and A. K. Agrawal, “Drop Size and Velocity Measurements in Bio-Oil Sprays Produced by the Flow-Blurring Injector,” in *Proceedings of ASME Turbo Exp 2011, June 6-10*, 2011, vol. GT2011-468, no. 2, pp. 1–10.

[18] E. Johnson, V. Srinivasa n, P. J. Strykowski, and A. Hoxie, “Role of Density in Gas-Assist Counterflow Atomization,” *ILASS-Americas 30th Annu. Conf. Liq. At. Spray Syst.*, no. May, pp. 1–7, 2019.

[19] A. Hoxie, E. Johnson, V. Srinivasan, and P. Strykowski, “Characteristics of a novel energy-efficient atomizer employing countercurrent shear,” *14th Int. Conf. Liq. At. Spray Syst.*, pp. 1–9, 2018.

[20] P. J. Strykowski and D. L. Niccum, “The stability pf countercurrent mixing layers in circular jets,” *J. Fluid Mech.*, vol. 227, no. 5, pp. 309–343, Apr. 1991.

[21] D. J. Forliti, B. A. Tang, and P. J. Strykowski, “An experimental investigation of planar countercurrent turbulent shear layers,” *J. Fluid Mech.*, vol. 530, pp. 241–264, 2005.

[22] M. Provansal, C. Mathis, and L. Boyer, “Benard - von Karman instability : transient and forced regimes,” *J. Fluid Mech.*, vol. 182, pp. 1–22, 1987.

[23] D. M. Kyle and K. R. Sreenivasan, “The instability and breakdown of a round variable-density jet,” *J. Fluid Mech.*, vol. 249, pp. 619–664, 1993.

[24] M. P. Hallberg and P. J. Srykowski, “On the universality of global modes in low-density axisymmetric jets,” *J. Fluid Mech.*, vol. 569, pp. 493–507, 2006.

[25] R. Govindarajan and K. C. Sahu, “Instabilities in viscosity-stratified flow,” *Annu. Rev. Fluid Mech.*, vol. 46, no. 1, pp. 331–353, Jan. 2014.

[26] P. A. Monkewitz, P. Huerre, and J.-M. Chomaz, “Global linear stability analysis of weakly non-parallel shear flows,” *J. Fluid Mech.*, vol. 251, no. 1, p. 1, Apr. 1993.

[27] B. Pier and P. Huerre, “Nonlinear self-sustained structures and fronts in spatially developing wake flows,” *J. Fluid Mech.*, vol. 435, pp. 145–174, Jun. 2001.

[28] J.-M. J.-M. Chomaz, “Global instabilities in spatially developing flows: Non-normality and nonlinearity,” *Annu. Rev. Fluid Mech.*, vol. 37, no. 1, pp. 357–392, Jan. 2005.

[29] A. A. Behrens and P. J. Strykowski, “Controlling Volumetric Heat Release Rates in a Dump Combustor Using Countercurrent Shear,” *AIAA J.*, vol. 45, no. 6, pp. 1317–1323, 2007.

[30] D. Fuster *et al.*, “Instability regimes in the primary breakup region of planar coflowing sheets,” *J. Fluid Mech.*, vol. 736, pp. 150–176, 2013.

[31] Y. Ling, D. Fuster, G. Tryggvason, and S. Zaleski, “A two-phase mixing layer between parallel gas and liquid streams: Multiphase turbulence statistics and influence of interfacial instability,” *J. Fluid Mech.*, vol. 859, pp. 268–307, 2019.

[32] E. Johnson, Vinod Srinivasan, P. J. Strykowski, and A. Hoxie, “Influence of Injection Gas Molar Mass on Counterflow Atomizer Performance.”

[33] B. C. H. Jr and E. F. Patton, “Surface Tensions of Propylene Glycol + Water,” *J. Chem. Eng. Data*, vol. 37, pp. 331–333, 1992.

[34] K. Takamura, H. Fischer, and N. R. Morrow, “Physical Properties of Aqueous Glycerol SOlutions,” *J. Pet. Sci. Eng.*, vol. 98–99, pp. 50–60, 2012.

[35] K. S. Kim and S.-S. Kim, “Drop sizing and depth-of-field correction in TV imaging,” *At. Sprays*, vol. 4, no. 1, 1994.

[36] K. U. Koh, J. Y. Kim, and S. Y. Lee, “Determination of in-focus criteria and depth of field in image processing of spray particles,” *At. Sprays*, vol. 11, no. 4, 2001.

[37] "OpenFOAM | Free CFD Software | The OpenFOAM Foundation," https://openfoam.org/